Numerical Heat Transfer, Part A, 41: 245–262, 2002

1040-7782/02 $12.00 + .00

TWO-DIMENSIONAL NUMERICAL VERIFICATION OF THE UNSTEADY THERMOACOUSTIC FIELD INSIDE A RIJKE-TYPE PULSE COMBUSTOR

Behnam Entezam and William K. Van Moorhem
Department of Mechanical Engineering, University of Utah, Salt Lake City, Utah, USA

Joseph Majdalani
Department of Mechanical & Industrial Engineering, Marquette University, Milwaukee, Wisconsin, USA

In this article a numerical model is developed to investigate the thermoacoustic conversion of heat into sound in a Rijke tube. This study is carried out in an attempt to better understand the internal coupling among heat addition, pressure, and velocity oscillations inside a Rijke-type pulse combustor. In fact, similar coupling is believed to exist in other combustion devices including rocket motors at the verge of instability. In light of the recent progress in computational fluid dynamics (CFD), we are now able to incorporate the compressibility and acoustic wave effects bridging the gap between thermal and pressure oscillations. When acoustic velocity and pressure have favorable time phases in the lower tube section, their synchronously alternating motions in the upward or downward directions give rise to acoustic excitation. As a result, an optimal conversion occurs whereby thermal energy is converted into mechanical energy. The latter is manifested in the form of acoustic intensity, a by-product of acoustic velocity and pressure. Below a threshold value in power input to the internal heat source, no self-sustained acoustic oscillations are observed. Conversely, when a critical power input to the heater is exceeded, resonance is triggered in the form of pronounced acoustic amplification. Self-sustained thermal oscillations near the heat source are found to be responsible for driving the acoustic pressure excitation. The acoustic pressure and velocity mode shapes along the centerline concur with one-dimensional acoustic theory except near the heater source where a local increase in the velocity amplitude is noted. Our two-dimensional CFD results agree with experimental observations reported in other studies. During limit-cycle oscillations, the acoustic pressure is found to lead thermal fluctuations by a 45-degree angle. This result may be used to specify the phase angle in Carvalho's analytical formulation, which predicted a value smaller than 90 degrees. Overall, numerical results indicate a strong pressure dependence on heat fluctuations. In fact, the modulus of thermal oscillations is found to be directly proportional to the modular product of acoustic velocity and pressure. In relation to solid and hybrid rocket motors, our findings can be extrapolated to predict a strong thermoacoustic, noise generating coupling in the forward half of the motor.

Received 18 January 2001; accepted 29 August 2001.

The authors wish to thank the editor and anonymous referees, whose help is most gratefully acknowledged.

Address correspondence to Professor J. Majdalani, Department of Mechanical & Industrial Engineering, Marquette University, 1515 W. Wisconsin Ave., Milwaukee, WI 53233, USA. E-mail: joseph.majdalani@marquette.edu

NOMENCLATURE

A	oscillatory pressure amplitude	T	temperature
a_0	mean speed of sound inside the Rijke tube	u'	oscillatory velocity component
		x	axial distance measured from the bottom
C_p	constant pressure specific heat	γ	mean ratio of specific heats
l	internal tube length	ρ	air density
m	longitudinal oscillation mode, $m = 1, 2, 3, \ldots, \infty$	ω	circular frequency, $m\pi a_0/l$
p'	oscillatory pressure component		
q	heat transfer rate, dQ/dt	**Subscripts**	
q'	oscillatory heat transfer rate	0	mean value
Q	heat energy	obs	obstacle or heat source
t	time	∞	surrounding mean flow condition

INTRODUCTION

Consider an open-ended circular tube held vertically. Inserting a steady heat source some short distance from the bottom of the tube produces large sound pressure levels that can be heard from a far distance. This phenomenon occurs inside the thermoacoustic pipe known as the Rijke tube. The mechanisms inside this device leading to the implicit conversion of heat fluctuations into acoustic energy has fascinated scientists for many years now. Due to their relevance to a number of practical applications, Rijke tube studies have received much scrutiny [1–14]. To supplement previous investigations that primarily have concentrated on theoretical and experimental studies, we undertake a computational verification of the Rijke tube's thermofluid character. To that end, we use the improved computational tools available today to develop a two-dimensional compressible flow model that is capable of pairing both thermal and fluid flow components of the problem. Our main interest is to determine how accurate numerical simulations can be, if possible at all, in reproducing the phenomena observed in the Rijke tube. In similar applications of oscillatory motions in thermoacoustic stacks, two-dimensional simulations that incorporate compressibility effects have been proven to be successful by Worlikar et al. [15, 16]. Another goal here is to help verify or establish missing terms in the mathematical equations that may be used later to obtain a complete closed-form solution. Aside from the scientific merit associated with achieving a numerical verification using modern computational tools, the results are hoped to help, in small part, further the development of a self-contained mathematical model. In this numerical study, no attempts will be made to obtain an analytical solution for the resulting model.

Another motivation for this study is the increased freedom and flexibility in varying the problem's physical parameters. In view of wider-range numerical experiments that are now possible, we hope to gain some insight into the physics underlying the thermoacoustic phenomena in pulse combustors in general.

To set the stage, we begin with a brief classification of three types of pulse combustors. This is followed by a description of the self-excited oscillator that defines the character of the Rijke tube. Next, the main features of the computational model are explained. Forthwith, results are presented and shown to concur with

existing experimental and theoretical predictions. In addition to providing an independent verification of the Rijke character, results will be used to help clarify some existing speculations. As a windfall, they seem to provide solutions to some unresolved terms arising in former analytical models.

CLASSIFICATION

The classic pulse combustors [17, 18] can be subdivided into three categories, depending on their acoustic mode shape configuration: (a) the closed–open, quarter-wave instrument known as the Schmidt tube; (b) the closed–open or open–open system known as the Helmholtz resonator; and (c) the open–open, half-wave system known as the Rijke tube. The latter denotes a vertical tube that comprises a single heat source and two isobaric ends.

The Rijke Tube

The earliest accounts of thermoacoustic oscillations can be traced to Rijke [19] in 1859. In his work, Rijke reported that strong oscillations could occur when a heated wire screen was placed in the lower half of an open-ended vertical pipe (see Figure 1*a*). These acoustic oscillations were found to stop altogether when the top end of the pipe was sealed. This indicated that upward convective air currents inside the pipe were essential for thermoacoustically driven oscillations to take place. As we can infer from Figure 1*a*, the Rijke tube is a half wave pulse combustor with an acoustic wavelength that is actually twice the length of the tube. Based on laboratory observations, we find that oscillations reach maximum amplification when the heater is centered in the bottom half. At that location, the pumping-like motions of acoustic pressure and velocity occur in the same direction. This favorable coupling gives rise to acoustic growth. For heater positions in the upper half of the pipe, the converse is true, and damping instead of driving occurs. Rijke believed that rising convection currents expanded in the region of the heated screen and were compressed downstream of the heater due to cooling at the pipe walls. These successive expansions and contractions were believed to be the cause for the intense production of sound. The reason is this: In the Rijke tube, the obstacle grid (gauze, screen, or heat source) heats the surrounding air and causes it to rise. Acoustically induced particle displacements are superimposed on the naturally convected steady flow. When acoustic particle displacements are positive upward, fresh cold air crosses the heated grid, but when negative, hot air from above is filtered through. During the upward motion, maximum heat transfer occurs between the heat source and the air due to the large temperature difference between the source and the cooler air. Since the timing in the acoustic cycle is such that maximum heat transfer corresponds to a positive particle displacement (with favorable upward motion), an ideal situation is created to promote acoustic wave growth according to Rayleigh's criterion [19]. In fact, the latter predicts acoustic excitation when heat is added to an acoustic wave at the high temperature phase of its cycle.

If the grid is now placed in the upper half of the pipe, acoustic velocity and pressure exhibit unfavorable phases. Pressure acts adversely, in a direction that opposes particle motion. Under such conditions, acoustic amplification is

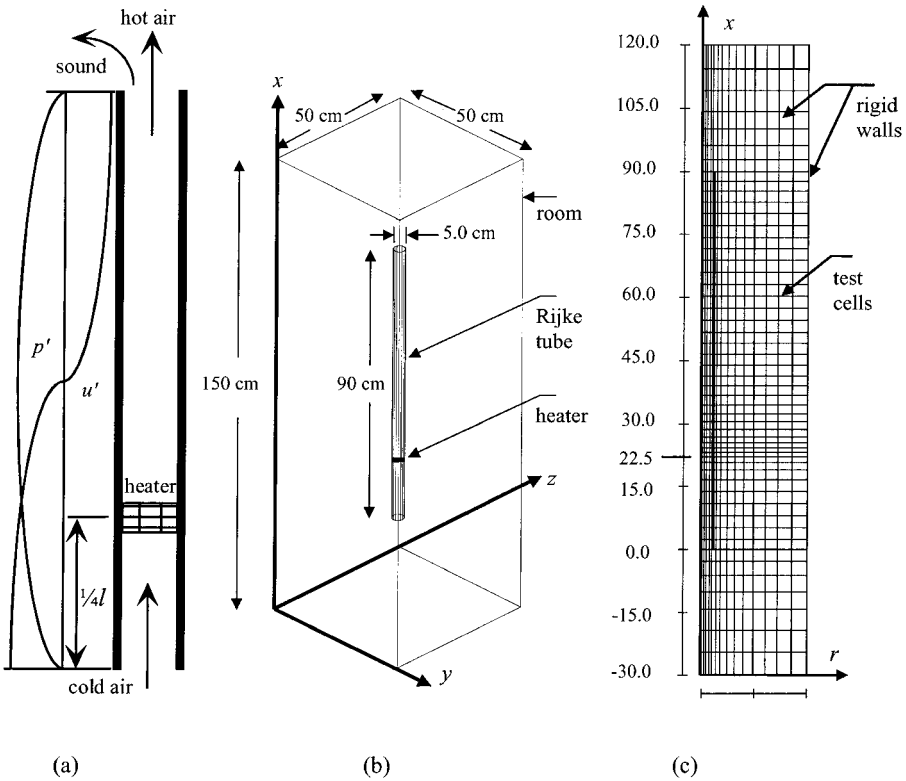

Figure 1. Schematic of the Rijke tube's (*a*) fundamental acoustic wave structure, (*b*) three-dimensional representation inside a room, and (*c*) computational mesh used in this study.

suppressed. If the phase between pressure and heat release rate is favorable, acoustic amplitudes increase, disturbances gain energy, grow in magnitude, and may lead to undesirable structural vibrations.

A Self-Excited Oscillator

For the Rijke tube, the wave equation can be written with the heat addition term acting as a driving function. To illustrate the basic source of coupling, the following simplified expressions may be used for both acoustic pressure and velocity [20]:

$$\frac{1}{a_0^2}\frac{\partial^2 p'}{\partial t^2} - \nabla^2 p' = \frac{1}{C_p T_0}\frac{\partial q'}{\partial t} \tag{1}$$

$$\frac{\partial^2 u'}{\partial t^2} - a_0^2 \nabla^2 u' = \frac{1-\gamma}{\rho_0}\frac{\partial q'}{\partial x} \tag{2}$$

In a self-excited oscillator, the energy associated with motion is supplied by a time-dependent quantity that is modulated by the oscillator itself. This quantity can be a force, an electric current, or a heat source, depending on the case at hand. Since the

unsteady driving term q' that appears in Eqs. (1)–(2) is induced by fluctuations in other thermodynamic quantities within the system, the Rijke tube is of the self-excited type. As it could be seen in Eqs. (1)–(2), the quest for analytical solutions to the problem requires that we know the functional form of q' beforehand. Furthermore, conditions controlling the flowfield on both sides of the heat source must be carefully posited. Determination of q' and its relation to p' and u' is hence desirable. Due to the absence of closed-form expressions linking p', u', and q', one of our goals will be to provide a physical explanation of the pertinent coupling based on numerical simulations.

THE COMPUTATIONAL MODEL

The Rijke tube is modeled as a pipe that is 90 cm in length and 5 cm in diameter. Only one cross section of the pipe is modeled, thus taking advantage of geometric symmetry. Figure 1*b* gives a three-dimensional rendering of the Rijke tube that is modeled as a hollow cylinder inside a room. The computational mesh in the $r - x$ directions is illustrated in Figure 1*c*. The domain comprises half of the Rijke tube and surrounding space. Ambient atmospheric conditions, including pressure, temperature, and density, are used to define the initial conditions at the tube's inlets and outlets, and inside the box representing the room. Note that the room itself does not constitute part of the numerical domain, but its properties are used to specify the parameters needed to simulate the convection heat transfer from the pipe walls to the surroundings. Because the radiation mode is of secondary importance, we ignore it.

To introduce an actual heat source, a horizontal porous obstacle with a diameter of 3.75 cm is inserted into the tube at a distance of 22.5 cm (i.e., $\frac{1}{4}l$) from the bottom. Thermostatic properties of steel are assigned to the obstacle whose surface porosity is assumed to result in a 90% open area fraction. The impact of this value on the thermoacoustic character is found to be secondary as long as the flow circulation in the tube remains unrestricted. The 90% value is chosen because it corresponds to the open area of realistic heated screen used in experimental investigations of the Rijke tube [21]. To preclude numerical instabilities associated with sudden parametric jumps, heat is linearly augmented inside the obstacle from zero to its specified value during the first two seconds of the simulation. After effectuating this gradual increase in a short period of time, the rate of internal heat generation is maintained constant for the remainder of the simulation.

Numerical Strategy

The numerical procedure involves two successive and equally important stages. The first stage is transient-like and carries the problem from an initial state of rest to a time of 20 seconds. After the first 20 seconds, the problem reaches a terminal or limit-cycle condition. Within numerical uncertainty, the terminal or quasi-steady-state oscillations exhibit constant amplitudes.

The second stage carries the problem from 20 to 20.025 seconds using a much smaller time step. The increased time resolution is necessitated by the need to track minute temporal changes in the acoustic waves. Throughout the tube, virtual probes are placed at several locations to monitor pressures, temperatures, densities, and

Table 1. Standard input properties

Obstacle (heat source)		
Material	—	Steel
Diameter	cm	3.75
Thickness	cm	1.0
Location from bottom	cm	22.5
Porosity	—	0.9
Power input	W	430
Thermal conductivity	W/m/K	36
Thermal capacitance	$J/m^3/K$	3.77×10^6
Heat transfer coefficient	$W/m^2/K$	calculated
Initial temperature	K	293.0
Gas		
Gas medium	—	Air
Gas constant	J/Kg/K	287
Dynamic viscosity	kg/m/s	1.824×10^{-5}
Specific heat	J/kg/K	718
Thermal conductivity	W/m/K	0.0251
Initial temperature	K	293.0

velocities. Our primary input variables and numerical parameters are summarized in Tables 1 and 2, respectively. This information is fed into the preprocessor of the input code of a commercially available software program developed for the analysis of fluid dynamic and thermal phenomena [22]. The software package consists of four separate programs. First, the preprocessor program translates input data into a useful problem description that can be interpreted by the main processor. Second, the main processor carries out the algorithms necessary for generating solutions under a wide range of physical conditions. The main processor exhibits a control

Table 2. Numerical parameters used in the code

Standard Settings for stage I
- Number of cells in x-direction, NXCELT = 16
- Number of cells in z-direction, NZCELT = 51
- Initial time step, DELT = 0.001 s
- Problem time to end calculation, TWFIN = 20.0 s
- Number of materials (air and pipe), NMAT = 2
- Gravity component in z-direction, GZ = $-$ 980 cm/s^2
- Automatic pressure iteration convergence adjustment for finer convergence, EPSADJ = 0.25
- Compressible flow option enabled, ICMPRS = 1
- Implicit pressure-velocity coupling enabled, IMP = 1
- Wall shear stress enabled, IWSH = 1
- Factor to improve convective stability, CON = 0.25
- Heat transfer evaluation paired with conduction equation, IHTC = 2

Modifications for stage II
- Continue calculations from stage I, TREST = 20.0 s
- Maximum permitted time step size, DTMAX = 0.0025 s
- Problem time to end calculation, TWFIN = 20.025 s

logic that aids in the selection of convergence criteria and time step sizes that help eliminate numerical instabilities. Third, the postprocessor enables the user to extract data, manipulate calculations, and format the plots needed to summarize the results acquired. Geometrical configurations are constructed by assembling solid geometric objects, or obstacles, which, when added together, define the flow region. The flow geometry is then embedded in the computational grid by defining the fractional areas of the grid cells open to flow and the corresponding fractional volumes that are open. All equations are formulated with area and volume porosity functions. The scheme is known as the fractional area-volume obstacle representation (FAVOR). It is intended to model complex geometric regions. Accordingly, all area-volume fractions are time independent.

Simulated Equations

The general continuity equation used in the program can be written as

$$V\frac{\partial \rho}{\partial t}+\frac{\partial}{\partial x}(\rho u A_x)+R\frac{\partial}{\partial y}\left(\rho v A_y\right)+\frac{\partial}{\partial z}(\rho w A_z)+\xi\frac{\rho u A_x}{x}=0 \tag{3}$$

where V is the fractional volume open to flow, ρ is the fluid density, and (A_x, A_y, A_z) are the fractional areas open to flow in the x, y, and z directions. The coefficients R and ξ, on the other hand, depend on the coordinate system. Next, the equations of motion for the fluid velocity are the Navier–Stokes equations augmented by some corrective terms. These are

$$\frac{\partial u}{\partial t}+\frac{1}{V}\left(uA_x\frac{\partial u}{\partial x}+vA_y R\frac{\partial u}{\partial y}+wA_z\frac{\partial u}{\partial z}\right)-\xi\frac{A_y v^2}{xV}=-\frac{1}{\rho}\frac{\partial p}{\partial x}+G_x+f_x-b_x \tag{4}$$

$$\frac{\partial v}{\partial t}+\frac{1}{V}\left(uA_x\frac{\partial v}{\partial x}+vA_y R\frac{\partial v}{\partial y}+wA_z\frac{\partial v}{\partial z}\right)+\xi\frac{A_y uv}{xV}=-\frac{1}{\rho}R\frac{\partial p}{\partial y}+G_y+f_y-b_y \tag{5}$$

$$\frac{\partial w}{\partial t}+\frac{1}{V}\left(uA_x\frac{\partial w}{\partial x}+vA_y R\frac{\partial w}{\partial y}+wA_z\frac{\partial w}{\partial z}\right)=-\frac{1}{\rho}\frac{\partial p}{\partial z}+G_z+f_z-b_z \tag{6}$$

where (G_x, G_y, G_z) are body accelerations, (f_x, f_y, f_z) are viscous accelerations, and (b_x, b_y, b_z) are flow losses across the porous baffle plates. For compressible and thermally buoyant flow problems, the internal energy equation becomes

$$\begin{aligned}V\frac{\partial}{\partial t}(\rho I)+\frac{\partial}{\partial x}(\rho I u A_x)+R\frac{\partial}{\partial y}\left(\rho I v A_y\right)+\frac{\partial}{\partial z}(\rho I w A_z)+\xi\frac{\rho u A_x}{x}\\ =-p\left[\frac{\partial(uA_x)}{\partial x}+R\frac{\partial(vA_y)}{\partial y}+\frac{\partial(wA_z)}{\partial z}+\xi\frac{uA_x}{x}\right]+\text{TDIF}\end{aligned} \tag{7}$$

where $I = C_V$ is the macroscopic mixture internal energy assumed to be a linear function of temperature, and C_V is the specific heat at constant volume. Heat conduction is accounted for in the term for diffusion (TDIF).

Since the heat transfer option is selected in the input code, dynamic temperatures of solid structures are evaluated. Solid structures can be either mesh wall boundaries or obstacles. The most general equation solved for the dynamic temperature of solid structures is

$$\rho_w C_w \partial T_w / \partial T + \nabla \cdot (K_w \nabla T_w) = \text{TSOR} \tag{8}$$

where T_w is the solid structure temperature while ρ_w, C_w, and K_w represent the solid material values for density, specific heat, and thermal conductivity. The term for solid obstacle representation (TSOR) is an energy source term composed of contributions from user-specified external sources and solid–liquid interactions. In our problem, this term accounts for the heat generated at the obstacle.

Heat transfer coefficients are evaluated using simple correlations appropriate of heat convection from flat surfaces. The correlations implemented are based on four physical situations: natural convection, forced laminar convection, forced turbulent convection, and conduction within the fluid. Leaning toward the conservative side, we evaluate all correlations and adopt the largest value, as prescribed by the program algorithm. Using standard notation, we see that these correlations correspond to

$$\text{Nu} = \begin{cases} 0.57\ (\text{Gr}\,\text{Pr})^{1/4} & \text{Gr}\,\text{Pr} \le 10^9 \\ 0.14\ (\text{Gr}\,\text{Pr})^{1/3} & \text{Gr}\,\text{Pr} > 10^9 \end{cases} \quad \text{(natural covection)} \tag{9}$$

$$\text{Nu} = 0.664\ \text{Pr}^{1/3}\ \text{R}_e^{1/2} \quad \text{(forced laminar convection)} \tag{10}$$

$$\text{Nu} = \text{Pr}^{1/3}\ (0.036\text{R}_e^{0.8} - 836) \quad \text{(forced turbulent convection)} \tag{11}$$

$$h = \frac{k(\partial T/\partial s)}{T_w - T_f} \quad \text{(fluid conduction)} \tag{12}$$

The nondimensional quantities in these expressions are given by the Nusselt, Prandtl, Reynolds, and Grashof numbers; namely,

$$\text{Nu} = hL/k \quad \text{Pr} = C_p\mu/k \quad \text{R}_e = \rho u L/\mu \quad \text{and} \quad \text{Gr} = g\beta\left|T_w - T_f\right|L^3(\rho/\mu)^2 \tag{13}$$

The code solves the foregoing equations using finite volume and finite difference approximations. Since our flow is compressible, the continuity equation is solved as a parabolic equation (i.e., by a marching algorithm in time). The pressure is then determined by requiring the equation of state density to equal the updated cell density. The flow region is subdivided into a mesh of fixed rectangular cells. With each cell, one associates average values of all dependent variables. Variables are located at the centers of the cells except for velocities; these are located at the cell faces. Curved obstacles, wall boundaries, and other geometric features are embedded in the mesh by specifying the fractional areas and fractional volumes of the cells that are open to flow. To construct discrete numerical approximations to the governing equations, control volumes are defined surrounding each variable location. For all control volume surface fluxes, surface stresses and body forces are computed in

terms of surrounding variable values. These quantities are then combined to form approximations for the conservation equations. Most terms in the equations are evaluated using the current time level values of the local variables. This produces a simple and efficient (explicit) computational scheme for most purposes, but requires the use of a limited time step size to maintain computationally stable and accurate results. One important exception to this explicit formulation arises in the treatment of pressure forces. In fact, pressures and velocities are coupled implicitly by using time-advanced pressures in the momentum equations and time-advanced velocities in the continuity equation. This semi-implicit formulation of the finite difference equations leads to an efficient solution of the low speed and incompressible flow problems. In our application where a more implicit solution method is required, a special alternating direction, line implicit method is used.

RESULTS AND DISCUSSION

A number of parametric studies are carried out in an attempt to characterize the internal flow field. This is done after refining the grid to the point at which changes in the solution become insignificant. A benchmark case is first selected with typical physical dimensions and thermodynamic properties. The acoustic character is analyzed and compared with both experimental and theoretical predictions. After setting up the proper boundary conditions, the temporal evolutions of mean and acoustic variables are tracked. The location and power supply to the heater source are varied separately to assess their influence on the solution. Whenever possible, the coupling between thermal and acoustic variables is reported.

Benchmark Case

To set a benchmark, a standard case is defined whose properties correspond to a typical Rijke tube, heat source power input, and gas properties. As posted in Table 1, our benchmark case is a standard run that involves a steady heat release of 430 watts at an optimal heater position of $\frac{1}{4}l$ from the bottom. Results are summarized in Figures 2–4.

In Figure 2*a*, temporal plots are shown, during the first 20 seconds, for pressure, axial velocity, temperature, density, and heat transferred to the air. The rate of heat transferred to the air q is a function of the obstacle temperature T_{obs}, temperature of ambient air T_∞, surface area of the source A_{obs}, and average heat transfer coefficient $\bar{h}$. It is defined according to Newton's cooling law, namely, $q = \bar{h}A_{\text{obs}}(T_{\text{obs}} - T_\infty)$.

Note that, after about 8.5 seconds, heat, pressure, and velocity oscillations begin. This threshold coincides with the time when the air temperature around the source begins to approach its terminal condition. This condition is signaled by the leveling out of the temperature curve in Figure 2*a*. In that region, small temperature oscillations occur but are too small to be discerned without scale magnification (see Figure 2*b*). As the temperature of the air increases, both pressure and velocities increase as well. This is accompanied by a decline in density as the heated gas expands. Since no acoustic pressure growth occurs prior to the temperature reaching its limit-cycle oscillations, it may be inferred that thermal

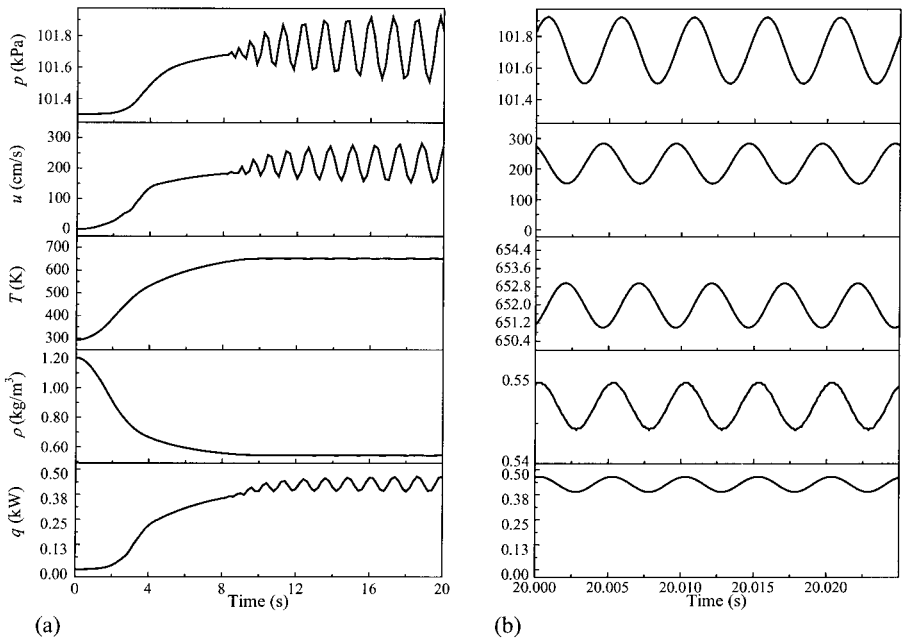

Figure 2. Time evolution of pressure, axial velocity, temperature, density, and heat transfer during (*a*) stage I, and (*b*) stage II. This benchmark case corresponds to a power input of 430 watts supplied to a heat source at $x = \frac{1}{4}l$.

fluctuations at the heater location are the main driving factor in producing the acoustic excitation. In a sense, the Rijke tube may be likened to a thermoacoustic pump in which the pumping-like temperature oscillations raise the acoustic energy to markedly audible levels.

The physics underlying these observations may be attributed to the following. As the source temperature begins to rise, a temperature difference between the source and surrounding air is created on both sides of the obstacle surface. The reduced density of the surrounding air causes it to stratify. Natural convection currents are hence produced due to buoyancy. As the heated air rises, it crosses the porous obstacle. The heat transferred from the source to the surrounding air can be determined to be a function of source temperature, ambient air temperature, source area, and average convection heat transfer coefficient. Since all properties are intimately related, the slightest disturbance in a given quantity is echoed in the signals obtained from the remaining variables. The acoustically driven motion is hence established once temperature oscillations become self-sustained.

Figure 2*b* displays temporal plots of pressure, axial velocity, temperature, density, and heat transferred to the air for the limit-cycle oscillation stage (20 to 20.025 seconds). Here, a smaller time step is utilized to track the acoustic growth more effectively. Clearly, Figure 2*b* indicates that periodic oscillations are present in all flow variables at a frequency of about 200 Hz. This reassuring frequency matches very closely the acoustically prescribed natural frequency, $f = ma_0/(2l)$, for the fundamental oscillation mode ($m = 1$) in a pipe with isobaric ends.

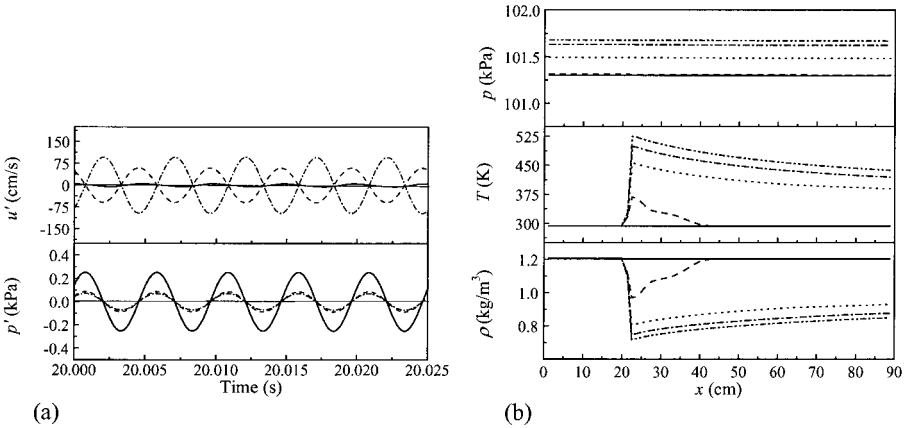

Figure 3. Here we show (*a*) the acoustic pressure and axial velocity at three key locations corresponding to $x = \frac{1}{2}l$ (—), $\frac{1}{16}l$ (- - -), and $x = \frac{15}{16}l$ (– – –); and (*b*) the spatial distribution of steady pressure, temperature, and density at several times before the inception of oscillations. Starting from rest, time evolutions are shown at discrete steps corresponding to $t =$ ——0; – – – 2; - - - 4; – - - - 6; – - - -8 s.

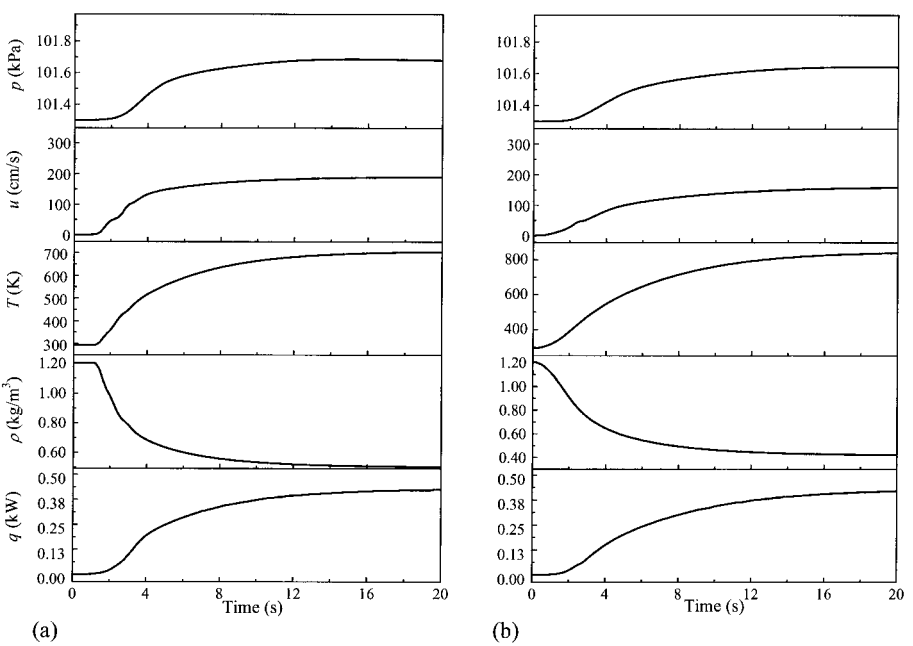

Figure 4. Time evolution of pressure, axial velocity, temperature, density, and heat transfer during the first 20.0 seconds of the numerical simulations. Keeping the power input at the benchmark value of 430 watts, we can now move the heater to (*a*) $x = \frac{1}{2}l$ and (*b*) $x = \frac{2}{3}l$. Clearly, oscillations are suppressed when moving away from the optimal quarter length location.

The Tube's Finite Length

To capture the acoustic mode shapes due to the pipe's finite body length, we use Figure 3*a* to illustrate the pressure and axial velocity oscillations at several different locations along the pipe. An examination of Figure 3*a* suggests that pressure oscillations reach their maxima at the center of the pipe and are small near both ends. Also, pressure oscillations appear to be in phase at any axial location, as one would expect from acoustic wave theory. The velocity plot, on the other hand, shows that velocity oscillations reach their maxima near both ends and are near zero at the center of the pipe. As such, velocity oscillations are 180° out of phase in the lower and upper half-domains. These results exhibit the expected patterns predicted by acoustic theory. Surely, they are also in agreement with experimental observations in Rijke tubes [1, 3, 4, 6, 14].

Boundary Conditions

One side benefit of numerical experiments is that they can help complete a mathematical model by helping to identify the necessary boundary conditions. This may be accomplished by verifying the types of auxiliary conditions that are necessary for a successful assault on the problem. In our case, pressure, temperature, and density distributions had to be carefully selected at key locations for $t < 0$. Subsequently, from $t = 0$ until the oscillations began, the evolution of the primary thermodynamic variables had to be tracked numerically along the length of the tube. Results obtained are shown in Figure 3*b* for the three principal variables. Note, in particular, the temporal solution across the heat source where abrupt changes take place. Prior to the inception of thermoacoustic oscillations, the pressure is almost constant along the pipe. The temperature remains constant in the lower section of the tube also. Its amplitude experiences a sudden jump upon crossing the source. This is followed by a rapid decay due to mixing with the unheated air.

The density variation shows that air expands after crossing the heat source. The similar but inverted functional form exhibited by the density may be anticipated from the ideal gas equation. Results provide numerical predictions for local flow properties, especially at both ends of the heat source.

Relocating the Heat Source

During separate numerical runs, the source is relocated to the middle $\left(\frac{1}{2}l\right)$ and to the upper section $\left(\frac{2}{3}l\right)$ of the pipe. This is done to observe whether oscillations would occur. Figures 4*a*–4*b* are graphical representations of the pressure, axial velocity, temperature, density, and source heat transfer versus time at the $\frac{1}{2}l$ and $\frac{2}{3}l$ heater locations. The location of the heat source seems to be a key factor in producing large amplitude oscillations. When the source is positioned at $\frac{1}{2}l$, no oscillations are seen. The same can be said when the source is at $\frac{2}{3}l$. When the source is placed in the lower half of the pipe, however, large amplitude oscillations are triggered. The resulting oscillations are found to have the largest amplitudes when the source is located at $\frac{1}{4}l$ from the bottom end. This is in accord with experimental findings reported previously [1, 3, 4, 6, 14]. Conclusively, oscillations occur only in the regions where acoustic velocity and pressure couple favorably such as in the

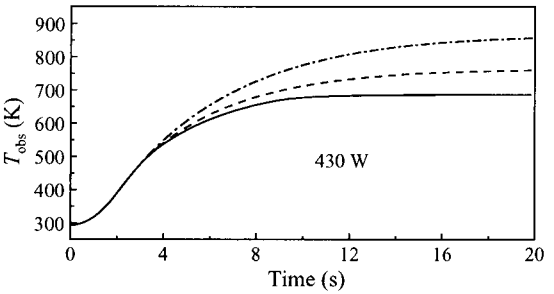

Figure 5. Time evolution of the surface temperature for the heat source when located at $x = \frac{1}{4}l$ (—), $x = \frac{1}{2}l$ (– – –), and $\frac{2}{3}l$ (– - –).

lower half of the tube (see Figure 1*a*). This pairing occurs when the pumping motions of both acoustic pressure and velocity take place in the same direction. In fact, maximum growth is noted where the modular product of acoustic pressure and velocity is maximized.

Figure 5 describes the temporal evolution of the source temperature T_{obs} at several locations. It can be observed that the heat source has a lower temperature when placed at $\frac{1}{4}l$ than at $\frac{1}{2}l$ and $\frac{2}{3}l$. The observation of a lower surface temperature at the $\frac{1}{4}$ location is accompanied by the maximum acoustic amplification recorded in the Rijke tube. Consequently, the heater location that produces the maximum acoustic energy appears to coincide with the point where the maximum amount of energy is converted to acoustic pressure intensity. In conjunction with the maximum conversion of thermal energy into sound, it is unsurprising that the temperature of the obstacle at $\frac{1}{4}l$ is minimized. A similar thermal character has been reported in coal-fired gas turbines [23, 24].

Varying the Heat Power Input

While the standard conditions stated above are retained, we vary the heat power input to the source. Keeping the source at the ideal $\frac{1}{4}l$ position, we release several heat power levels of 125.5, 376.6, 408.0, 426.9, 430.0, 433.1, and 439.4 watts. The effect of varying the heat input on the induced acoustic motion can thus be captured.

Figure 6 is a graphical representation of the pressure for the first 20 seconds. For sufficiently small input (e.g., 125.5 W or below) no sign of oscillations can be detected. We infer that the heat input level, which feeds the acoustic oscillations, must possess some low threshold value. For the benchmark case chosen here, we find that self-sustaining acoustic oscillations are established when the heat input exceeds a threshold value of 376 W. Below this value, no appreciable acoustic oscillations can occur. The breakdown in the oscillations at high powers (i.e., 433.1 and 439.4 W) signals the onset of acoustic resonance in the form of self-sustained, large amplitude oscillations. Clearly, the breakdown takes place sooner when a higher internal generation heat source is provided. This explains the shifting of the flat section in the pressure trace preceding the large amplitude oscillations in the last two insets of Figure 6.

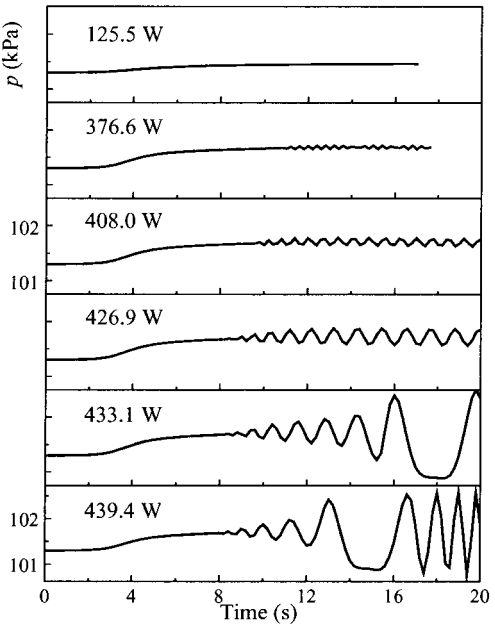

Figure 6. Time evolution of pressure for different power inputs (stage I). This a standard run with the heat source located at the optimal distance $x = \frac{1}{4}l$.

Our experiments suggest the presence of another critical value beyond which the acoustic growth becomes very pronounced. This is illustrated in Figure 7*a* where maximum pressure amplitudes are shown along with the sound pressure levels that accompany them. Clearly, large decibel levels are detected when the heat power input is in excess of 427 W. In fact, somewhere between 427 and 433 W, a sudden jump in the pressure output levels is observed with repeated runs. This phenomenon is akin to resonance and is reproducible at a critical heat power input of approximately 430 W.

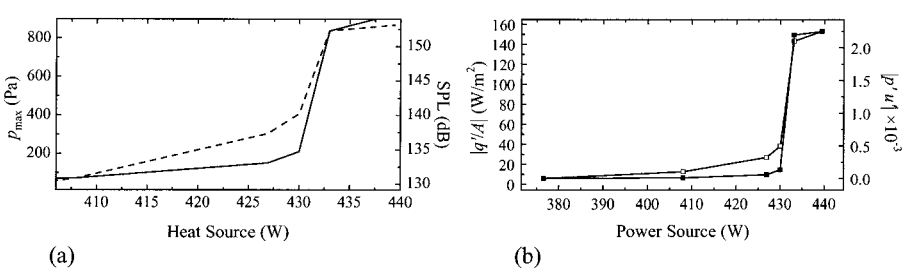

Figure 7. Plot of (*a*) maximum pressure (—) and corresponding sound pressure levels (- - -) for a range of heat power input levels. Note the sudden pressure jump near a critical power input of 430 W. In (*b*) the corresponding modular product of acoustic pressure and velocity (–□–) is compared with the modulus of heat oscillation flux (–■–).

Acoustic Pressure and Velocity Mode Shapes

Along the pipe's axis of symmetry, the acoustic pressure and velocity mode shapes obtained numerically are in general accord with one-dimensional, plane wave theory. As shown in Figure 8*a*, the oscillatory pressure reaches its maximum value at the center of the pipe and is a minimum near both ends. This mode shape concurs with classic theory. Likewise, acoustic velocity reaches its local maximum near both ends and is a minimum at the center of the pipe. This is also in agreement with acoustic theory. However, an interesting result can be seen in the velocity mode shape near the heater. There, a local distortion appears in the velocity amplitude. The increased local velocity can be ascribed to the strong coupling between velocity and thermal oscillations near the heater. In fact, recent articles by Prosperetti, Watanabe, Yuan, and Karpov have revealed similar mode shape behavior [25, 26]. In particular, Prosperetti and coworkers have been successful in developing analytical solutions that can accurately predict the complex behavior near the heat source. For a thorough theoretical description of thermoacoustic phenomena observed in Rijke tubes, the reader is referred to the fundamental analyses presented in Refs. [25–28].

Acoustic Phase Angles

Figure 8*b* shows the relationship among pressure, velocity, and heat transfer oscillations at the source. In concurrence with acoustic theory, the pressure leads the velocity oscillation by a 90° phase angle. Interestingly, we find that q' is leading u' by 45°, and lagging behind p' by the same amount. In a former study, Carvalho [3] had demonstrated that the phase between acoustic pressure and heat had to be less than 90°. His hypothesis is in agreement with our result, which suggests a phase lag of 45°. In supplementing Carvalho's analytical model, we now propose that a value of $\phi = \pi/4$ may be used in his expression for pressure oscillations. Repeated here for convenience, the pertinent equation reads

$$p' = A\sin\frac{m\pi x}{l}\sin(\omega t + \phi) \tag{14}$$

where ϕ is the phase lead between p' and q'.

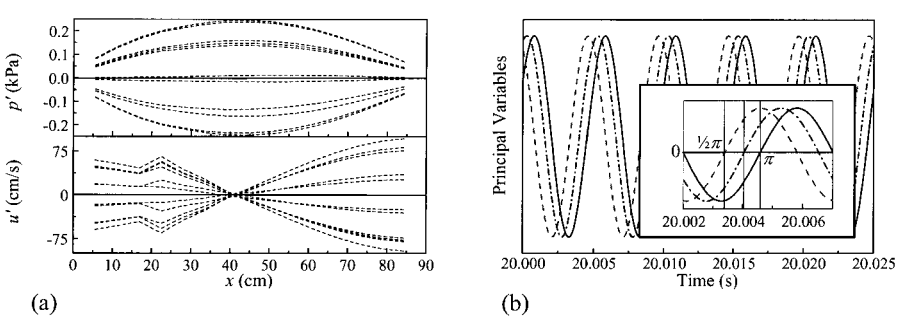

Figure 8. Plot of (*a*) acoustic pressure and velocity versus distance for several discrete times in a cycle. In (*b*), we show the relationship between acoustic pressure (—), axial velocity (- - -), and heat flux (– - –) at the optimal $x = \frac{1}{4}l$ location. Results in (*b*) correspond to the limit-cycle oscillations of stage II.

The Thermoacoustic Form of Coupling

Suspecting a relationship between thermal and mechanical energy (in the form of acoustic intensity, $p'u'$), we have decided to plot the modulus of heat oscillations alongside the modulus of the acoustic intensity. Based on our numerical simulations, the modulus of the heat oscillation q' appears to be proportional to the modular product of acoustic velocity and pressures $p'u'$. As shown in Figure 7*b*, there is a strong indication of an intimate coupling between q' and $p'u'$ in the standing wave field. Physically, these observations suggest that a direct conversion of heat into mechanical energy does exist. A simple expression for q' may be proposed. Owing to the fact that the heat at the source is produced per unit area, and for dimensional homogeneity, the constant cross-sectional flow area may be factored in. Thus one may write

$$|q'| \sim |p'u'|A \tag{15}$$

Equation (4) can be used in finding a solution to the set given by (1)–(2).

CONCLUDING REMARKS

The numerical results described above appear to be in good agreement with laboratory observations reported by other investigators. This is especially true when taking into consideration the experimental uncertainties associated with laboratory measurements. As such, they are supportive of a theory that attributes acoustic growth to the by-product of pressure and velocity interactions. Both experimental observations and present numerical solutions agree that, unless the pressure and velocity couple favorably, acoustic attenuation will prevail. Favorable coupling takes place when the temporal pumping-like motions of fluctuating pressure and velocity components occur synchronously in the same upward or downward directions. When thermal oscillations become self-sustained, acoustic pressure and velocity begin to grow in amplitude. When suitably paired, they lead to a strong acoustic amplification and a relatively large conversion of thermal energy into sound. The conversion of thermal energy into sound appears to be maximum at the heater location leading to the minimum surface temperature of the heating screen (i.e., at $\frac{1}{4}l$). Our study also suggests the presence of a minimum threshold value for the heat power supplied below which no self-sustained acoustic oscillations may be possible. In our numerical experiment, this value is 376 W. A critical value of the heat power input is also found to cause resonance to occur. When 430 W are supplied to the heater, a sharp peak in the acoustic amplitude is observed. Unsurprisingly, the resulting acoustic pressure and velocity mode shapes do concur with classic acoustic theory along the axis of the tube. Near the heater, however, a marked increase is noted in the velocity amplitude that eludes plane wave acoustic theory. This abrupt variation in velocity amplitude agrees with recent models developed by Prosperetti and coworkers. During limit-cycle oscillations, the acoustic pressure is found to lead thermal fluctuations by a 45-degree angle. The acoustic velocity also lags behind thermal fluctuations by the same amount. This numerically determined result helps complete Carvalho's solution. Finally, the modulus of heat oscillations is found, in all numerical experiments, to be proportional to the modulus of acoustic intensity.

REFERENCES

1. T. Bai, X. C. Cheng, B. R. Daniel, J. I. Jagoda, and B. T. Zinn, Vortex Shedding and Periodic Combustion Processes in a Rijke Type Pulse Combustor, *Comb. Sci. Tech.*, vol. 94, no. 1–6, pp. 245–258, 1993.
2. T. Bai, X. C. Cheng, B. R. Daniel, J. I. Jagoda, and B. T. Zinn, Performance of a Gas Burning Rijke Pulse Combustor with Tangential Reactants Injection, *Comb. Sci. Tech.*, vol. 94, no. 1–6, pp. 1–10, 1993.
3. J. A. Carvalho, C. Ferreira, C. Bressan, and G. Ferreira, Definition of Heater Location to Drive Maximum Amplitude Acoustic Oscillations in a Rijke Tube, *Comb. Flame*, vol. 76, no. 1, pp. 17–27, 1989.
4. R. E. Evans and A. A. Putnam, Rijke Tube Apparatus, *AJP*, vol. 34, pp. 360–361, 1966.
5. K. T. Feldman, Review of the Literature on Rijke Thermoacoustic Phenomena, *J. Sound Vib.*, vol. 7, pp. 83–89, 1968.
6. M. M. Friedlander, T. J. B. Smith, and A. Powell, Experiments on the Rijke Tube Phenomenon, *J. Acoust. Soc. Am.*, vol. 36, pp. 1737–1738, 1964.
7. G. C. Maling, Simplified Analysis of the Rijke Phenomenon, *J. Acoust. Soc. Am.*, vol. 35, pp. 1058–1060, 1963.
8. J. Miller and J. A. Carvalho, Comments on Rijke Tube, *Scient. Am.*, vol. 204, no. 3, pp. 180–182, 1961.
9. N. Miller, E. A. Powell, F. Chen, and B. T. Zinn, Use of Air Staging to Reduce the Nox Emissions from Coal Burning Rijke Pulse Combustors, *Comb. Sci. Tech.*, vol. 94, no. 1–6, pp. 411–426, 1993.
10. R. L. Raun and M. W. Beckstead, Numerical Model for Temperature Gradient and Particle Effects on Rijke Burner Oscillations, *Comb. Flame*, vol. 94, no. 1–2, pp. 1–24, 1993.
11. M.-R. Wang and B. T. Zinn, Controlling Processes in Rijke Type Coal Burning Pulsating Combustors, *Chem. & Phys. Processes in Comb.*, vol. 61, pp. 1–61, 1984.
12. M.-R. Wang and B. T. Zinn, Performance Characteristics of a Prototype, Rijke Type Pulsating Combustor, *J. Chinese Soc. Mech. Engrs.*, vol. 8, no. 5, pp. 339–345, 1987.
13. Z. X. Xu, D. Reiner, A. Su, T. Bai, B. R. Daniel, and B. T. Zinn, *Flame Stabilization and Combustion of Heavy Liquid Fuels in a Rijke Type Pulse Combustor: Fossil Fuel Comb.*, vol. PD 33, pp. 17–26, New York,1991.
14. B. T. Zinn, N. Miller, J. A. Carvalho, and B. R. Daniel, *Pulsating Combustion of Coal in a Rijke Type Combustor, Proceedings of the 19th International Symposium on Combustion*, pp. 1197–1203, 1982.
15. A. S. Worlikar, O. M. Knio, and R. Klein, Numerical Study of the Effective Impedence of a Thermoacoustic Stack, *Acoustica*, vol. 85, pp. 480–494, 1999.
16. A. S. Worlikar and O. M. Knio, Numerical Study of Oscillatory Flow and Heat Transfer in a Loaded Thermoacoustic Stack, *Numerical Heat Transfer Part A-Applications*, vol. 35, no. 1, pp. 49–65, 1999.
17. B. T. Zinn, *State of the Art Research Needs of Pulsating Combustion: Noise Control & Acoustics*, vol. 84-WA NCA-19, Washington, DC, 1984.
18. B. T. Zinn, *Pulse Combustion: Recent Applications and Research Issues: Proceedings of the 24th International Symposium On Combustion*, vol. 19,626, pp. 1297–1305, Sydney, Australia, 1992.
19. J. W. S. Rayleigh, *The Theory of Sound*, vol. 1–2, Chap. 1–2, Dover Publications, New York, 1945.
20. B.-T. Chu, *Stability of Systems Containing a Heat Source—The Rayleigh Criterion*, NACA, Research Memorandum 56D27, 1956.
21. J. Majdalani, B. Entezam, and W. K. Van Moorhem, *The Rijke Tube Revisited via Laboratory and Numerical Experiments*: AIAA 2001-2961, 2001.

22. *Flow-3D*, Flow–Science Incorporated, Los Alamos, NM, 1997.
23. G. A. Richards, R. G. Logan, C. T. Meyer, and R. J. Anderson, Ash Deposition at Coal-Fired Gas Turbine Conditions: Surface and Combustion Temperature Effects, *ASME J. Eng. Gas Turb. Power*, vol. 114, no. 1, pp. 132–138, 1992.
24. G. A. Richards, G. J. Morris, D. W. Shaw, S. A. Keeley, and M. J. Welter, Thermal Pulse Combustion, *Comb. Sci. Tech.*, vol. 94, no. 16, pp. 57–85, 1993.
25. H. Yuan, S. Karpov, and A. Prosperetti, A Simplified Model for Linear and Nonlinear Processes in Thermoacoustic Prime Movers. Part II. Model and Linear Theory, *J. Acoust. Soc. Am.*, vol. 102, no. 6, pp. 3497–3506, 1997.
26. M. Watanabe, A. Prosperetti, and H. Yuan, A Simplified Model for Linear and Nonlinear Processes in Thermoacoustic Prime Movers. Part II. Model and Linear Theory, *J. Acoust. Soc. Am.*, vol. 102, no. 6, pp. 3484–3496, 1997.
27. S. Karpov and A. Prosperetti, Linear Thermoacoustic Instability in the Time Domain, *J. Acoust. Soc. Am.*, vol. 103, no. 6, pp. 3309–3317, 1998.
28. S. Karpov and A. Prosperetti, Nonlinear Saturation of the Thermoacoustic Instability, *J. Acoust. Soc. Am.*, vol. 107, no. 6, pp. 3130–3147, 2000.